How *Euglena gracilis* swims: Flow field reconstruction and analysis

Nicola Giuliani,[1] Massimiliano Rossi,[3] Giovanni Noselli,[1] and Antonio DeSimone[1,2]
[1] *SISSA–International School for Advanced Studies, Via Bonomea 265, 34136 Trieste, Italy*
[2] *The BioRobotics Institute and Dept. of Excellence in Robotics and AI, Scuola Universitaria Superiore Pisa, Piazza Martiri della Libertà, 56127 Pisa, Italy*
[3] *DTU–Department of Physics, Technical University of Denmark, DTU Physics Building 309, DK-2800 Kongens Lyngby, Denmark*

(Received 12 October 2020; revised 16 January 2021; accepted 19 January 2021; published 8 February 2021)

Euglena gracilis is a unicellular organism that swims by beating a single anterior flagellum. We study the nonplanar waveforms spanned by the flagellum during a swimming stroke and the three-dimensional flows that they generate in the surrounding fluid. Starting from a small set of time-indexed images obtained by optical microscopy on a swimming *Euglena* cell, we construct a numerical interpolation of the stroke. We define an optimal interpolation (which we call synthetic stroke) by minimizing the discrepancy between experimentally measured velocities (of the swimmer) and those computed by solving numerically the equations of motion of the swimmer driven by the trial interpolated stroke. The good match we obtain between experimentally measured and numerically computed trajectories provides a first validation of our synthetic stroke. We further validate the procedure by studying the flow velocities induced in the surrounding fluid. We compare the experimentally measured flow fields with the corresponding quantities computed by solving numerically the Stokes equations for the fluid flow, in which the forcing is provided by the synthetic stroke, and find good matching. Finally, we use the synthetic stroke to derive a coarse-grained model of the flow field resolved in terms of a few dominant singularities. The far field is well approximated by a time-varying Stresslet, and we show that the average behavior of *Euglena* during one stroke is that of an off-axis puller. The reconstruction of the flow field closer to the swimmer body requires a more complex system of singularities. A system of two Stokeslets and one Rotlet, that can be loosely associated with the force exerted by the flagellum, the drag of the body, and a torque to guarantee rotational equilibrium, provides a good approximation.

DOI: 10.1103/PhysRevE.103.023102

I. INTRODUCTION

Euglenids are one of the best-known groups of flagellates and are easily found in freshwater [1]. Their biology and cellular structure is well known and over the last decade there has been a growing interest in studying the mechanics underlying their motility. An interesting feature is that Euglenids can exhibit distinct forms of motility (flagellar swimming and amoeboid motion), can switch between them [2], and respond to environmental cues such as confinement and light [3]. This makes them an interesting model system to study sensing and response mechanisms in an elementary, single-cell organism.

The amoeboid motion of Euglenids, typically referred to as metaboly, has been studied from an analytical [4], numerical [5], and experimental [2,6] perspective, and it has inspired the design of soft robots [7]. The flagellar swimming of *Euglena gracilis*, powered by the nonplanar beating of a single anterior flagellum, termed "spinning lasso" in the literature, has been studied for a long time, but a detailed experimental reconstruction of this complex kinematics has been obtained only recently and can be found in Ref. [8]. It is also known that the organism can modulate the beating of the flagellum to change its trajectory [3], also in response to external light stimuli. In fact, *E. gracilis* is phototactic.

The study of the flow fields induced by unicellular swimmers through their shape changes plays a key role in understanding the interactions of the cell with its living environment [9–13]. For example, predators may sense their preys through the flows they generate with their motion, or they may induce flows to drive preys towards their feeding organs and capture them (see, e.g., Refs. [14,15] and the references cited therein). The main features of all these flows can be rationalized by approximating them as the superposition of a few elementary singular solutions [16,17]. Many different organisms have been analyzed in this way in recent years. Bacteria exhibit mainly rotational flows near the cell body and a pusher flow far away from the cell [16]. As another example, *Chlamydomonas reinhardtii* produces flow fields of different character during its stroke, oscillating between pusher and puller behaviors, while in average it behaves as a puller [18]. The time-dependent features of the flow of sperm cells have been analyzed in Ref. [19]. Analyses of this type yield interesting insight in understanding the interactions between different swimmers [20] or between the swimmer and different interfaces [21–23].

Given the three-dimensional nature of the motion of the flagellum and the lack of obvious symmetries, resolving the flow fields induced by *Euglena* cells would be particularly interesting. The technical challenges involved have prevented this, at least until now. In fact, extending to three dimensions the two-dimensional results on trajectories and flows obtained in recent years is one of the frontiers in the research on the biophysics of microswimmers, as witnessed by the increasing focus on three-dimensional effects in the recent literature [8,13,24–28].

In this paper, we propose to use numerical simulations of the dynamics of swimmer and surrounding fluid to complement the experimental data and overcome some of the difficulties that have limited the study of the swimming behavior of *E. gracilis* so far. Our main results are the following. We provide a reconstruction of the swimming stroke in terms of shapes and of their rate of change and validate it by showing that the application of a hydrodynamic model to the theoretical flagellar waveforms produces swimming trajectories in close agreement with the experimentally observed ones. We further validate our reconstruction of the swimming stroke by computing the three-dimensional flows induced in the surrounding fluid, measuring them with particle tracking velocimetry techniques, and showing good match between the two. Finally, we provide a coarse-grained model of the fluid flows induced by a swimming *Euglena* in terms of a few dominant singularities. A time-varying Stresslet suffices to capture the far field, and the average behavior in one stroke is that of an off-axis puller (i.e., the axes of the puller flow are not aligned with the body axis). Closer to the swimmer body, a system of two Stresslets and one Rotlet is more appropriate to resolve the salient features of the induced flows, loosely associated with the forces exerted by the beating flagellum, the drag of the body, and a torque ensuring rotational equilibrium. In order to capture the fact that the forces exerted by the flagellum at any given time may change character from propulsive to resistive along the flagellum, an even more complex systems of singularities would be required.

A first attempt to reconstruct numerically the swimming behavior of *E. gracilis* has been performed in Ref. [8], using a method explored also in Ref. [24]. In Ref. [8] Resistive Force Theory (RFT) [29,30] is used to check the consistency of the experimentally measured trajectories with the motion arising as a consequence of the reconstructed flagellar beat. Quantitative discrepancies were attributed to the limitations of RFT when dealing with hydrodynamic interactions; see Refs. [31,32] for further details. In fact, the complex flagellar kinematics described in Refs. [8,25] requires more accurate models for the nonlocal hydrodynamic forces generated by a flagellum beating in close proximity of the cell body, and in the present work we address the problem using an open source boundary element method [33,34] that has been validated in a previous publication [32].

The rest of the paper is organized as follows. In Sec. II we confront the following problem: Starting from a set of time-indexed images defining the shapes during a stroke, and obtained by optical microscopy, determine the corresponding history of shape velocities (the rate at which shapes evolve in time). In the present work we focus our attention on the study of the flagellar shapes reported in Ref. [8]. Other beating patterns, such as those reported in Ref. [3], will be addressed in the future. We proceed by numerical interpolation in time and derive an optimized numerical interpolation of the stroke in the neighborhood of each experimental image by minimizing the discrepancy between experimentally measured translational and rotational velocity of the swimmer and those computed by solving the equations of motion of the swimmer driven by the interpolated shapes. In this way, we obtain pairs (shape, shape velocities) at each time frame, and hence a time-discrete numerical description of the stroke that we call synthetic stroke.

In Sec. III we validate the synthetic stroke by comparing the flow fields it induces, calculated by solving numerically the equations for the fluid flow, with experimental measurements. In order to measure the fluid velocities experimentally, we use the General Defocusing Particle Tracking (GDPT) method [35]. This technique allows for a three-dimensional reconstruction of the flow field looking at the displacement of out-of-focus tracer particles with a single-camera view. The defocusing is used to obtain the out-of-plane particles' position, and it is enhanced by using a cylindrical lens to induce a controlled optical aberration in the optical system [36]. We obtain full three-dimensional velocity fields, and then we use the azimuthal mean introduced in Ref. [37] to compare experimental observations with the numerical results obtained with our synthetic stroke.

Finally, in Sec. IV we analyze the flow fields induced by the flagellar beating of *E. gracilis* (modeled using our synthetic stroke). We coarse grain the flow field using Stokes flow singularities. This kind of analysis has been successfully applied to other swimmers such as *C. reinhardtii* [17,38], sperm cells [19,39], and bacteria [16,40]. The procedure extracts the essential characteristics of the flow by approximating it as the superposition of a few singular solutions of the Stokes equations.

We find that, not unlike other organisms [18], the far field is well described by a single time-varying Stresslet. This is confirmed by the analysis of the leading order term of a multipole expansion of the equation describing the flow field, following Ref. [41]. A swimming *E. gracilis* cell oscillates between puller and pusher behaviours and its average behavior over one stroke can be idealized as an off-axis puller, i.e., one in which the axes of the puller flow are not aligned with the longitudinal axis of the body.

To coarse grain the flow field at distances closer to the body of the swimmer we propose a system of singularities consisting of two Stokeslets and one Rotlet, and we show that this system performs better than other commonly used. The Stokeslets and Rotlet can be loosely associated with the propulsive (and resistive) forces exerted by the flagellum, the drag of the body, and a torque ensuring rotational equilibrium. We also show, however, that the flagellum may exert forces whose orientations and character at any given time may change along its length (e.g., propulsive forces near the proximal end and resistive ones at the distal end). The consequence of this fact is that, to properly resolve the flows induced in close proximity of the swimmer's body, more complex systems of singularities are needed, such as multiple Stokeslets along the length of the flagellum.

II. NUMERICAL RECONSTRUCTION OF A SWIMMING STROKE (SYNTHETIC STROKE)

This section aims at constructing a numerical representation of a swimming stroke starting from a finite set of time-indexed flagellar shapes obtained experimentally from a representative swimmer. The experimental procedure is described in detail in Ref. [8] and relies on high-speed video recordings of *Euglena* specimens swimming regularly[1] along a direction parallel to the microscope's focal plane. Due to specific symmetries in this system, we can exploit a fitting procedure to extrapolate from the microscopy recordings the trajectory and orientation of the swimmer body in space and time, and to resolve the 3D flagellar shape for a finite number of stroke positions. For the case at hand, considering a specimen swimming with a beating period $T_b = 24.3$ ms observed with a recording frequency of 1000 fps, it was possible to reconstruct 10 flagellar shapes. Detailed information on the accuracy and reproducibility of the reconstruction are given in Ref. [8].

The idea is to interpolate in time the experimentally obtained flagellar shapes and to choose an optimal interpolation capable of reproducing accurately the motion of the swimmer and the induced flows. We call this optimal interpolation synthetic stroke. This is obtained by minimizing the discrepancy between experimentally measured translational and rotational velocities of the swimmer and those computed by solving the equations of motion of the swimmer driven by the interpolated stroke.

The procedure we adopt is based on two key steps: (1) the mathematical definition and numerical solution of the swimming problem and (2) an optimization procedure to extrapolate flagellar shapes to pairs of flagellar shapes and shape velocities. The procedure leads to the definition of a numerical time-discrete synthetic stroke starting from a limited set of experimental observations.

A. Mathematical formulation of the swimming problem

We follow Refs. [42,43] to represent a model swimmer as a time-dependent bounded open set $B_t \in \mathbb{R}^3$. We describe the motion using the map $\chi : \bar{B}_0 \subset \mathbb{R}^3 \times [0, T] \rightarrow \mathbb{R}^3$ which carries a material point $\mathbf{X}$ of the swimmer into its current position $\mathbf{x}$ at time t,

$$\mathbf{x} = \chi(\mathbf{X}, t) = f_r(s(\mathbf{X}, t), t) = \mathbf{q}(t) + \mathbf{R}(t)[s(\mathbf{X}, t) - \mathbf{O}], \tag{1}$$

where bold symbols denote points, vectors, and tensors. According to Eq. (1), χ results from the composition of prescribed shape changes $s(\mathbf{X}, t)$ and a rigid motion f_r of translation $\mathbf{q}(t)$ and rotation $\mathbf{R}(t)$. We set $B_t = \chi(B_0, t)$; see Fig. 1. As for the velocity of any material point on $\Gamma = \partial B_t$, from (1) we obtain

$$\begin{aligned}\dot{\mathbf{x}} &= \frac{\partial \chi(\mathbf{X}, t)}{\partial t} \\ &= \dot{\mathbf{q}}(t) + \mathbf{R}(t)\dot{s}(\mathbf{X}, t) + \boldsymbol{\omega}(t) \wedge \{\mathbf{R}(t)[s(\mathbf{X}, t) - \mathbf{O}]\},\end{aligned} \tag{2}$$

where we have introduced the angular velocity $\boldsymbol{\omega}(t)$. Assuming that shape changes are prescribed through a periodic function of time, the unknowns of the swimming problem are $\dot{\mathbf{q}}(t)$ and $\boldsymbol{\omega}(t)$, which characterize the translational and rotational motion of the swimmer (referred to as the rigid velocities in what follows).

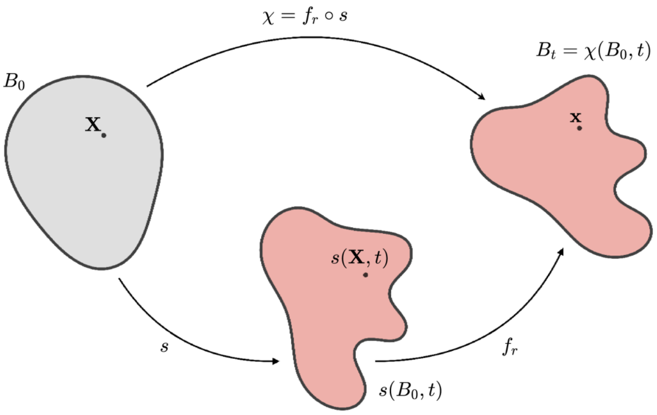

FIG. 1. A sketch of the swimmer motion $\chi(\mathbf{X}, t)$ to highlight its decomposition into prescribed shape changes $s(\mathbf{X}, t)$ and a rigid motion f_r.

In view of the characteristic length and time scales relevant to microswimmers, inertial effects are negligible such that the balance of linear and angular momentum read

$$\int_\Gamma \mathbf{f}(\mathbf{x}, t)\, d\gamma = 0, \quad \int_\Gamma \mathbf{f}(\mathbf{x}, t) \wedge (\mathbf{x} - \mathbf{O})\, d\gamma = 0, \tag{3}$$

where $\mathbf{f}(x, t)$ is the viscous traction acting on the boundary of the swimmer. This is given by the action of the Cauchy stress tensor $\boldsymbol{\sigma}$ [44],

$$\mathbf{f} = \boldsymbol{\sigma}(\mathbf{v}, p)\mathbf{n}, \tag{4}$$

where $\mathbf{n}$ is the outer unit normal to the boundary Γ, and $(\mathbf{v}, p)$ represent the velocity and pressure fields in the fluid. For an incompressible Newtonian fluid the Cauchy stress tensor is given by

$$\boldsymbol{\sigma}(\mathbf{v}, p) = \mu(\nabla \mathbf{v} + \nabla \mathbf{v}^T) - p\mathbf{I}, \tag{5}$$

so that, in the low-Reynolds number approximation of microhydrodynamics, fluid flow is governed by Stokes' equations [45]. Neglecting gravity (here we consider a neutrally buoyant swimmer) and assuming that the swimmer moves in free space, these read

$$\operatorname{div} \boldsymbol{\sigma} = \mu \Delta \mathbf{v} - \nabla p = 0\,, \quad \text{and} \quad \operatorname{div} \mathbf{v} = 0\,, \quad \text{in } \mathbb{R}^3 \setminus B_t. \tag{6}$$

These are complemented by no-slip boundary conditions at the swimmer boundary, where $\mathbf{v}$ must match the velocity of the swimmer given by (2), and decay conditions at infinity. Notice that the linearity of Stokes' equations leads to a linear dependence of the tractions $\mathbf{f}(\mathbf{x}, t)$ appearing in (3) on the shape velocities $\dot{s}(\mathbf{X}, t)$ (data) and on the rigid velocities $\dot{\mathbf{q}}(t)$ and $\boldsymbol{\omega}(t)$ (unknowns) appearing in (2). Solving (3) for the latter, we obtain the instantaneous translational and rotational velocities of the swimmer resulting from shapes changing at rate $\dot{s}$.

We solve numerically the Stokes system by exploiting a Boundary Element Method (BEM), and among the different possible implementations we follow Refs. [33,46]. Figure 2 shows the geometric BEM discretization of *Euglena* consisting of 1032 different cells. Further information about the numerical scheme are available in the Supplemental Material [47].

---

[1] We consider the specimen to swim *regularly* when it uses consecutive identical strokes, resulting in a helical motion around a straight screw axis.

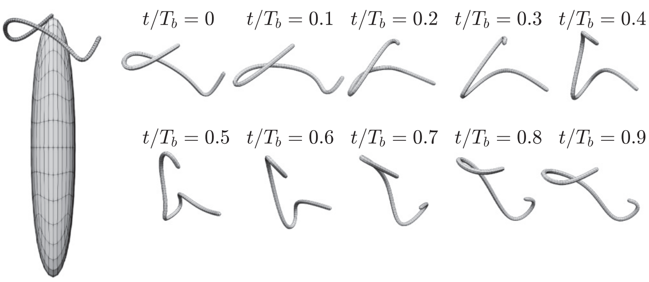

FIG. 2. Geometric reconstruction of *E. gracilis*: 384 cells constitute the cell body and 648 the flagellum. We report on the right the 10 flagellar shapes corresponding to the 10 times t used to discretize the beating period T_b in Ref. [8].

B. Optimal numerical interpolation based on experimental rigid velocities

The numerical procedure exploiting the BEM defines a unique map between the function giving the history of the shapes of the swimmer during one stroke and its rigid velocities (translational and rotational) during the stroke. In principle, we could write

$$s(\mathbf{X}, t) \xrightarrow[\text{differentiation}]{\text{numerical}} \dot{s}(\mathbf{X}, t) \xrightarrow[\text{resolution}]{\text{BEM}} \dot{\mathbf{p}}(t) \tag{7}$$

to obtain the rigid velocities $\dot{\mathbf{p}}(t) = (\dot{\mathbf{q}}(t), \boldsymbol{\omega}(t))$ from prescribed $s(\mathbf{X}, t)$.

In practice, information on the swimmer shapes is only available through finitely many snapshots coming from optical microscopy. For example, the experimental observations of Ref. [8] provide ten flagellar shapes during one stroke. However, as shown in Sec. II A, the rigid velocities of the swimmer, $\dot{\mathbf{p}}(t)$, can be computed by solving the equations of motion (3) only if the rate at which flagellar shapes change, $\dot{s}(\mathbf{X}, t)$, is known. The experimental observations of Ref. [8] do not provide this information, and we discuss now how we overcome this problem, by finding a suitable interpolation in time of the ten experimentally measured shapes.

Clearly, there are infinitely many interpolating paths. We reduce the degeneracy by exploiting the knowledge of the experimental values for the rigid velocities at the 10 instants at which flagellar shapes are known (Figs. 5(f) and 5(g) of Ref. [8]), and by defining an optimal interpolation that minimizes the discrepancy between experimentally measured translational and rotational velocities of the swimmer and those computed by solving the equations of motion (3) of the swimmer driven by the interpolated stroke. In this way, we obtain the pairs (shape, shape velocities) at each time frame, and hence a time-discrete synthetic stroke. The procedure is described in more detail below.

We consider the 10 flagellar shapes $\bar{s}(\mathbf{X}, t_i)$, $i = \{1, \ldots, 10\}$, reported in Ref. [8], and we interpolate them in time using spline interpolation. To this end, we introduce spline interpolants $g_j(\mathbf{X}, t)$ with degree $j = \{1, \ldots, N_g\}$. We fix the maximum degree $N_g = 5$ to obtain a good interpolation while limiting oscillating phenomena related to high order polynomials [48]. We reconstruct shapes as linear combinations of the N_g basis splines in a neighborhood of the 10 experimental frames,

$$s(\mathbf{X}, t) = \sum_{j=1}^{N_g} \alpha_{ij} g_j(\mathbf{X}, t), \quad t \in (t_i - \tau, t_i + \tau), \tag{8}$$

where α_{ij} are coefficients to be determined by best fit of the experimental data, and $\tau \ll t_{i+1} - t_i$ specifies the neighborhood of the experimental frame. To ensure that (8) interpolates the experimental flagellar shapes we require that $g_j(\mathbf{X}, t_i) = \bar{s}(\mathbf{X}, t_i)$ for all j, which is possible since $\bar{s}(\mathbf{X}, t_i)$ is given in Ref. [8] as a spline, and that

$$\sum_{j=1}^{N_g} \alpha_{ij} = 1. \tag{9}$$

We notice that

$$\dot{s}(\mathbf{X}, t) = \sum_{j=1}^{N_g} \alpha_{ij} \dot{g}_j(\mathbf{X}, t), \quad t \in (t_i - \tau, t_i + \tau), \tag{10}$$

and that we can associate some rigid linear and angular velocities to the basis shape velocities $\dot{g}_j(\mathbf{X}, t)$,

$$g_j(\mathbf{X}, t) \xrightarrow[\text{differentiation}]{\text{numerical}} \dot{g}_j(\mathbf{X}, t) \xrightarrow[\text{resolution}]{\text{BEM}} \dot{\mathbf{p}}_j(t) \text{ for } j = 1, \ldots, N_g. \tag{11}$$

By the linearity of the Stokes system it follows from (10) that

$$\dot{\mathbf{p}}(t_i) = \sum_{j=1}^{N_g} \alpha_{ij} \dot{\mathbf{p}}_j(t_i). \tag{12}$$

To determine the coefficients α_{ij} of the optimal interpolation (8) we require that

$$\dot{\mathbf{p}}(t_i) = \dot{\bar{\mathbf{p}}}_i, \tag{13}$$

where $\dot{\bar{\mathbf{p}}}_i$ is the value measured experimentally in Ref. [8] at the specific frame t_i. Notice that the set of experimental data comprises 6×10 rigid velocities and we use five different coefficients for 10 different time frames. We exploit a constrained least square minimization algorithm [49] to solve this overdetermined system and find values of α_{ij} fulfilling (9).

The results of the fitting procedure are shown in Fig. 3: Fig. 3(a) reports the linear velocities, whereas the angular velocities are shown in Fig. 3(b). Red triangles, green squares, and blue circles represent their components along the unit vectors of the body reference i, j, k. We plot with empty markers the results of the optimal spline interpolation, and we compare them with the reconstruction of Ref. [8], represented with filled markers. Remarkable agreement is found between our current methodology and the reference results. As for the components ω_x and ω_y of the angular velocity, these are recovered with slightly less accuracy. This minor difference is due to the fact that those two components are the ones with the lowest magnitude and consequently are less relevant in the least square resolution of (13) with constraint (9).

In order to define the trajectory associated with the synthetic stroke, we construct a continuous approximation of $\dot{\mathbf{q}}$ and $\boldsymbol{\omega}$ by using a Fourier expansion of the BEM data. We remark that this is consistent with the procedure used in Ref. [8] for the reconstruction of the experimental data. The continuous approximations are shown as continuous, dashed-dotted,

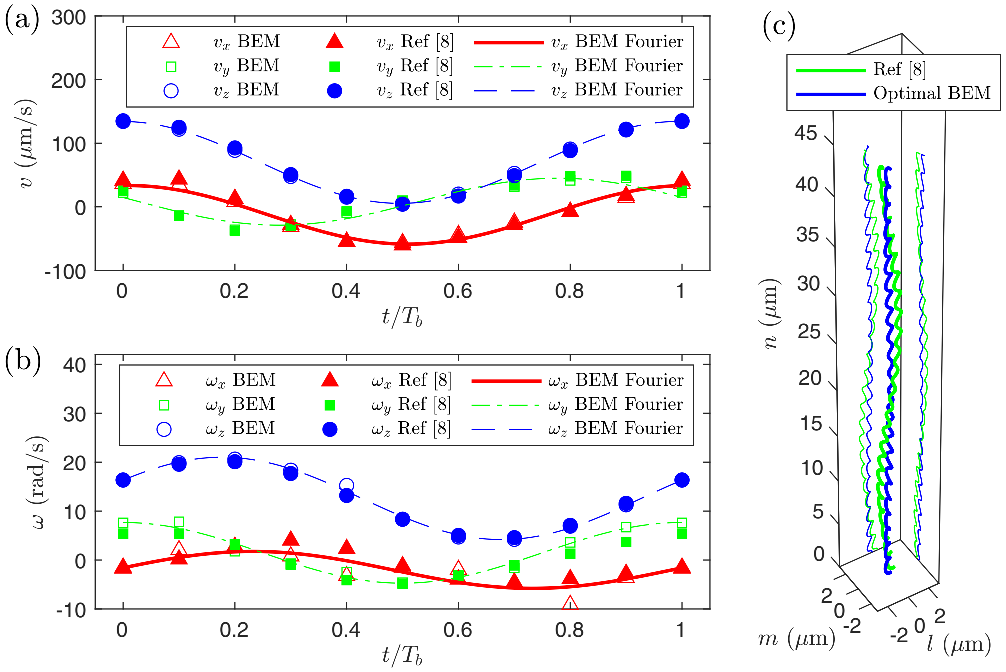

FIG. 3. Results of the fitting procedure: (a) and (b) represent linear and angular velocities, respectively. Triangles, squares, and circles refer to the component along i, j, k, respectively. Filled markers represent the experimental result reported in Ref. [8] while empty symbols are current BEM computations. Continuous, dashed-dotted and dashed lines are the Fourier continuation of the BEM optimal results we use to compare the trajectories in (c). (c) Comparison between the reference trajectory of Ref. [8] (in light green) and the trajectory from the optimal BEM solution (in dark blue) in a reference frame whose vertical axis is aligned with the average direction of motion.

and dashed lines in Figs. 3(a) and 3(b). We use a standard numerical integration to get the trajectory associated with our synthetic stroke (giving the optimal numerical time interpolation of the observed swimmer shapes), and we compare it with the experimental observations of the real swimmer in Fig. 3(c). Good agreement between our numerical reconstruction and the experimental observations is found also in terms of integrated trajectories.

Once the pairs (shape, shape velocities) defining a time-discrete synthetic stroke are known, one can use the BEM-based algorithm not only to compute translational and rotational velocity of the swimmer, but also to evaluate the velocity field at any point of the fluid domain $\mathbb{R}^3 \setminus B_t$. We remark that the presence of physical walls, needed in the experimental setting, does not seem to play a very significant role in the current analysis. In fact, *Euglena* swims with its longer body axis parallel to the walls (slide and coverslip) and in the transversal direction the diameter of the body (9 μm) is about one tenth of the channel width (80 μm). At these distances, the flow velocity computed form the free-space solution has decayed to 10% of the average swimming velocity (the rigid translational velocity). To double check that the presence of the walls does not alter significantly the conclusions of our analysis, we have computed the rigid velocities associated with our synthetic stroke in the presence of two no–slip walls, located at the same distance as in experimental setting, and we have found that the velocities variations over the stroke are, depending on the velocity component, between 1.7% and 16.5%. We conclude that, in agreement with Ref. [8], walls do not play a major role in the observed swimming behavior of *Euglena*.

In what follows, we use the flow velocity fields computed numerically from our synthetic stroke for further validation and analysis. In particular, in Sec. III we use the comparison of fluid flow velocities measured experimentally with those calculated from the synthetic stroke to confirm the reliability of the synthetic stroke. In Sec. IV we use the flow fields reconstructed numerically from the synthetic stroke to extract the main qualitative features of *Euglena*'s swimming stroke.

III. EXPERIMENTAL VALIDATION OF THE SYNTHETIC STROKE

As discussed earlier, BEM computations allow for the determination of the three-dimensional flow field induced by a swimming *Euglena* at given instants in the stroke with a degree of detail which is difficult to achieve experimentally. Nevertheless, an experimental validation of the velocity fields obtained numerically is required to validate the results of a computational model. Conventional 2D particle tracking velocimetry (PTV) has been used in the past to measure the flow field around microswimmers [14,50,51]. Due to its inherent limitations, this technique allows to measure only the components of the velocity parallel to the focal plane, with no information about the azimuthal velocity component [37]. To overcome these limitations, we rely here on the GDPT method [35] to measure the full 3D flow field around a swimming *Euglena*. To the best of our knowledge, this is the first time that 3D PTV measurements around a swimming micro-organism of this kind have been performed. To compare with the numerical results, we follow the approach proposed in Ref. [37] and consider time- and azimuthally averaged velocity fields,

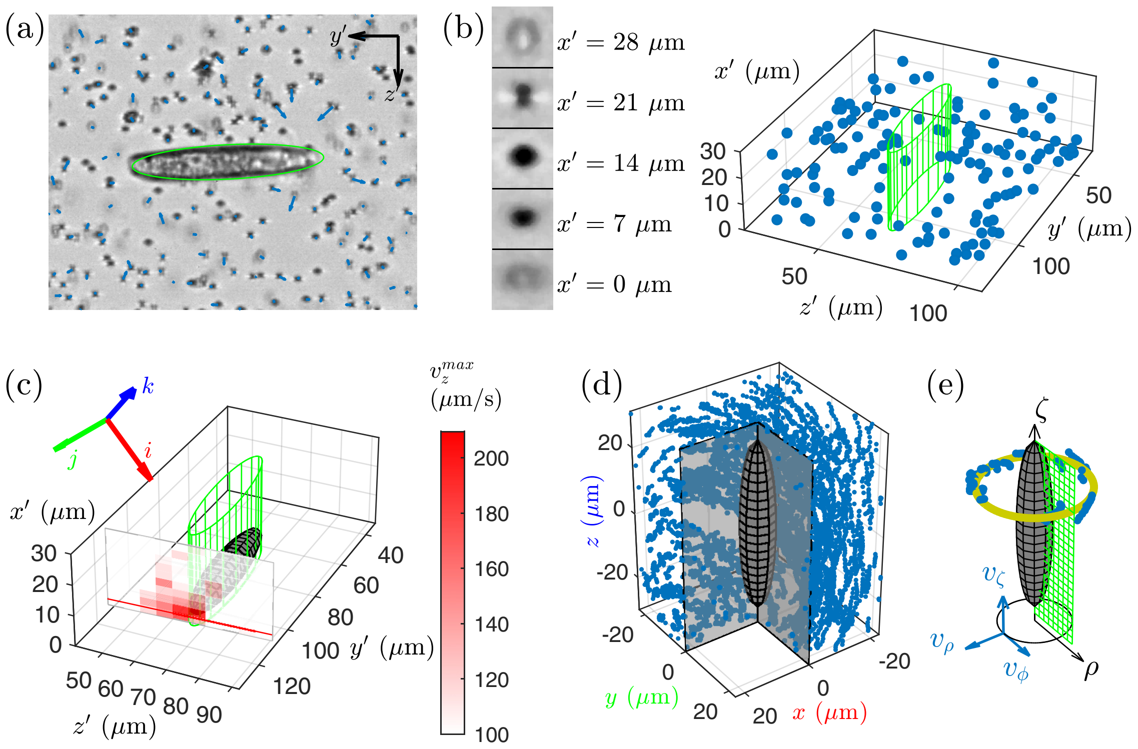

FIG. 4. (a) Micrograph of a swimming *Euglena* surrounded by tracer particles obtained with 64× magnification and astigmatic optics. (b) Reconstruction of 3D particle positions using the GDPT method. The depth position of tracer particles is determined from the different shape of the defocused-astigmatic particle images. (c) Determination of the depth position of the swimmer by looking at the maximum axial velocity of the fluid in the swimmer wake. (d)–(e) Determination of the time and azimuthally averaged velocity components. All particle positions and velocities are reported in the coordinate frame of the swimmer (ijk) and converted in cylindrical coordinates. The time and azimuthally averaged velocity components v_ρ, v_ζ, and v_ϕ are calculated as a function of ρ and ζ.

but this time accounting for all the velocity components, i.e., the radial, the vertical, and the azimuthal component. From now on we indicate with x, y, z the coordinates in the body reference frame identified by three unit vectors i, j, k, and with x', y', z' the coordinates in the laboratory frame.

A. Velocity measurements using general defocusing particle tracking (GDPT)

GDPT is a single-camera method that allows to measure the position in space of monodisperse tracer particles observed with an optics with small depth of field [52]. The corresponding particle images recorded with such a systems show distinctive defocusing patterns that depend on the particle position along the optical axis. To enhance the shape deformation and break the symmetry of the defocusing function along the depth direction, we used a cylindrical lens in front of the camera sensor to introduce a mild astigmatic aberration in the optical system [36,53]. GDPT is based on a look-up table approach to classify the particle-image defocusing patterns in relation to the particle depth position. The normalized cross-correlation is used to rate the similarity between target particle images and the reference images in the look-up table, and hence determine their respective depth position [54]. An exemplary micrograph with defocused particle images observed with the astigmatic optics and the respective 3D particle position reconstruction performed by GDPT is reported in Figs. 4(a) and 4(b). Clearly, particles in the image region occupied by the cell body could not be processed. The tracer particles are polystyrene beads with diameter of 1 μm (Life Technologies, catalog number F8821) at low concentration (volume fraction of 0.06%). A complete description of the experimental setup can be found in the Supplemental Material [47].

With the current setup we obtained a measurement volume of $168 \times 147 \times 28$ μm^3, with an estimated uncertainty in the determination of the particle position of 0.02 μm (0.15 pixels) for the in-plane coordinates and of 0.2 μm for the out-of-plane coordinate. As for the uncertainty in the velocity, this is affected by several factors: the particle positioning error, the time interval between two images (1 ms), and the Brownian motion of the particles. We estimated this uncertainty looking at particles in regions of stagnant fluid, obtaining values of 30 μm/s for the in-plane velocity components and of 120 μm/s for the out-of-plane component. These are of the order of magnitude of the velocities to be measured. For this reason, it was not possible to achieve time-resolved velocity fields and we had to consider smoothed time- and space-averaged data. It should be mentioned that other experimental techniques have been proposed to measure weak time-dependent flows around microswimmers, most notably optical tweezers [55,56]; however, they would require to immobilize the swimmer, which is not possible in our experiments.

For each experimental recording, the 3D trajectory and orientation of the cell was obtained using the procedure described in Ref. [8], except for the depth position. In fact, this was determined by looking at the maximum axial velocity

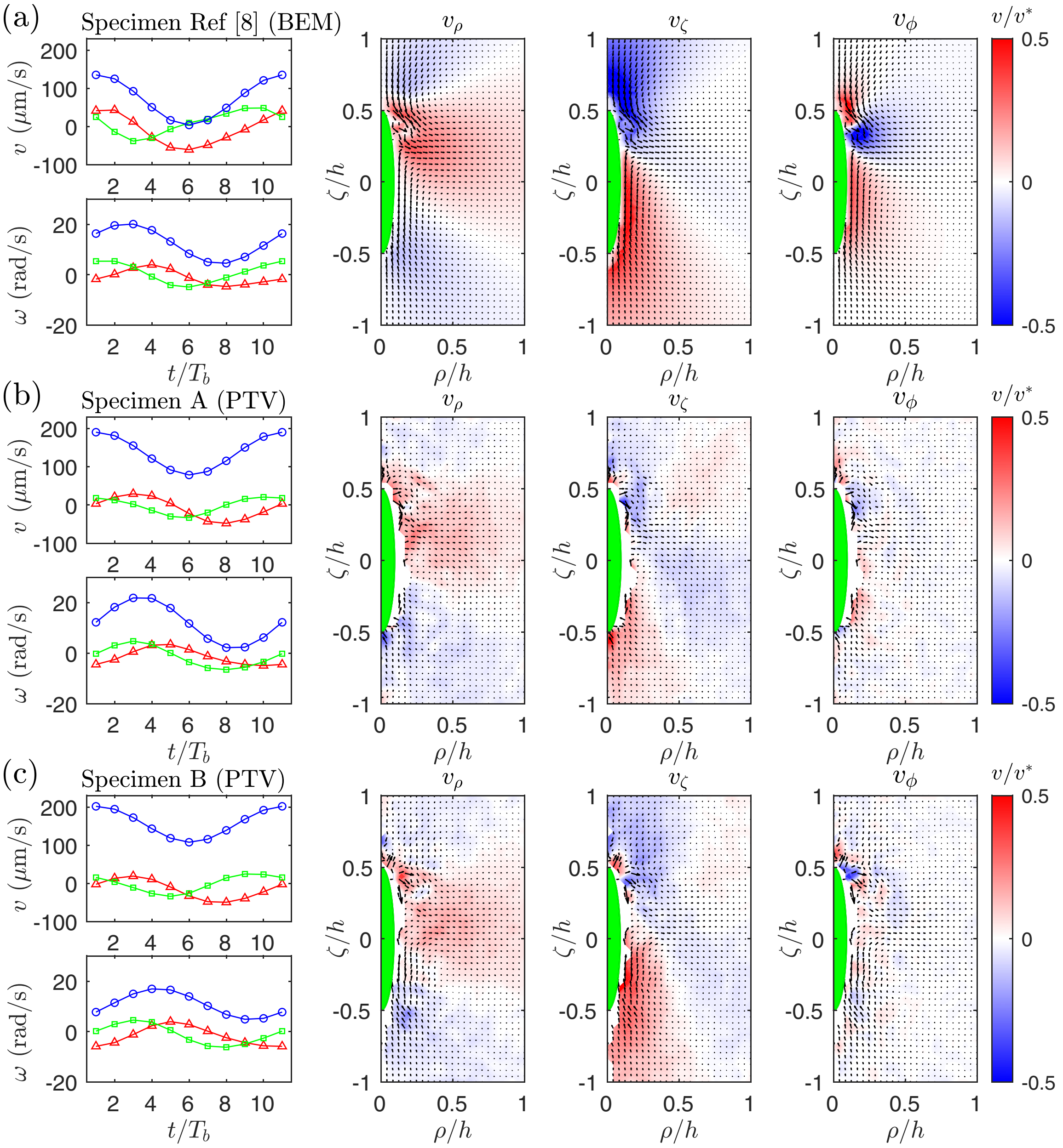

FIG. 5. Fluid flow comparisons in which each row shows results from a different specimen. The first column reports the body linear and angular velocities (lines with triangles, squares, and circles represent i, j, k components in body frame). The remaining three columns depict the different axisymmetrically projected velocities v_ρ, v_ζ, v_ϕ. The colormap is normalized using the mean velocity of the swimmer during the stroke v^*.

component ($v_z^{\max}$) of the flow field in a plane perpendicular to the cell body axis and just behind it; see Fig. 4(c). Under the approximation that the cell was swimming parallel to the image plane, the depth position could be identified by the point of maximum average velocity. With the knowledge of cell position and orientation, the velocity vectors measured by GDPT were reported in the reference frame of the cell [Fig. 4(d)] so that the cylindrical components of the flow velocity field around a swimming cell could be computed as defined in Fig. 4(e). In the figure, v_ζ denotes the vertical component, v_ρ the radial component, and v_ϕ the azimuthal component. Finally, the time- and azimuthally averaged velocity components were reported on a regular grid with pitch 1/48 of the swimmer length (pitch size of approximately 1 μm). At each point of the grid, velocity components were computed as based, on average, on 40 velocity samples, leading to a final estimated uncertainty of about 5 μm/s in the radial and vertical direction and of 18 μm/s in the azimuthal direction.

B. Comparison between experimental and numerical velocity flow fields

We report in Fig. 5 a comparison between the numerical reconstruction and the experimental results for the average flow field around the swimmer body. We represent two different experimental specimens to better identify the characteristic structures of the flow. It should be noted that a thorough analysis of the variance of flagellar beating geometries of *E. gracilis* specimens was performed in Ref. [8]. Such analysis showed that, beside some variability in the kinematic parameters, there is no substantial differences in the beating patterns of different specimens. The first column in the figure shows the linear and angular velocities of the cell body within a stroke. Clearly, the results relative to the specimen from Ref. [8], used as reference for the numerical reconstruction of Sec. II, and those from the experimental observation of other two samples share common distinctive features. For instance, the different components of linear and angular velocity appear in phase, a fact that allows for the comparison of velocity fields from different specimens. This is reported in the other columns of the figure in terms of the velocity components relevant to the axisymmetric projection: v_ρ, v_ζ, v_ϕ. In the three columns, we identify structures that appear to be characteristic of the average flow field around a swimming *Euglena*. Specifically, all the scalar fields can be subdivided in three different regions of alternating positive and negative sign. Furthermore, the fields in the second and third columns (i.e., those for v_ρ and v_ζ) clearly exhibit the behavior of a puller swimmer: the fluid is pulled by the swimmer at the top (negative v_ζ) and at the bottom (positive v_ζ), while it is pushed radially at the center (positive v_ρ). We note, in passing, that some differences emerge with respect to a typical puller, which is characterized by zero longitudinal velocity at $\zeta/L_{\text{body}} = 0$. The fact that, in the current analysis, v_ζ is different from zero (mainly negative) at these locations suggests that the pulling forces are at an angle with respect to the body axis of the swimmer. This feature, which is due to the intrinsic lack of symmetry in the flagellar beat of *Euglena*, was already observed in Ref. [51]. We will return to it in the next section.

The component v_ϕ of the velocity field (fourth column in Fig. 4) depends strongly on the rotation of the swimmer about its major axis. This can be described as a counterclockwise rotation around the body axis oriented from the posterior to the anterior end. We identify two positive regions at the top and at the bottom, and this observations agrees with the direction of rotation of the swimmer. Moreover, the asymmetric beating of the flagellum induces a rotational flow localized at the flagellum, and rotations of the body of opposite sign, which in turn induce a counter-rotating flow around the body. The negative tangential velocity in the central part of the body is consistent with the existence of this counter-rotating flow.

While the measured components of v_ρ and v_ζ compare well with the corresponding computed fields, a comparison for the component v_ϕ is more delicate. To understand why, we recall that Stokes flow can be coarse grained by using fundamental solutions of the Stokes system; the basic Stokes singularity associated with rotations is the so-called Rotlet, which induces a quadratic flow decay with the distance from the location of the singularity. Since the beating of the flagellum leads to the presence of two counter-rotating flows, the velocity component v_ϕ exhibits a cubic decay (we will investigate this aspect in more detail in Sec. IV). This rapid decay leads to a very low intensity of the signal to be measured. This fact, combined with the lower resolution of GDPT for the out-of-plane velocity component with respect to in-plane ones, implies a lower signal to noise ratio in the field v_ϕ with respect to the fields v_ρ and v_ζ. In spite of this, we are still able to identify the three different regions highlighted by the computational analysis, confirming that the flow structures identified by the BEM are characteristic of the real flow field around a swimming *Euglena*.

We conclude that the synthetic stroke defined in Sec. II approximates well not only the rigid body kinematics (linear and angular velocities, and trajectories of the cell body) but also the essential characteristics of the flow fields induced in the surrounding fluid.

IV. COARSE GRAINING THE FLOW FIELD

We move now to the analysis of the flow field induced by a swimming *Euglena*. A natural approach to study the swimming behavior of microswimmers is to consider the leading order term of the multipole expansion corresponding to the boundary integral equation. This approximation is expected to well represent the flow induced by a swimmer in the far field, and it provides useful insights about the swimming strategy that *Euglena* adopts. Following Refs. [41] and [18], we introduce the dipole matrix **D**, which represents the leading order term of the multipole expansion for the operators appearing in the representation formula of the Stokes system,

$$\mathbf{D}(t) = \int_\Gamma (\mathbf{x} - \mathbf{O}) \otimes \mathbf{f}(\mathbf{x}, t)\, d\gamma, \tag{14}$$

where $\mathbf{f}$ is the traction acting at place $\mathbf{x}$ of the boundary Γ of the swimmer's body. We then introduce the Stresslet matrix **S** as

$$\mathbf{S}(t) = \tfrac{1}{2}[\mathbf{D}(t) + \mathbf{D}^T(t)] - \tfrac{1}{3}\mathrm{Tr}(\mathbf{D})\mathbf{I}, \tag{15}$$

which can be computed by means of the BEM. As explained in Ref. [18], the determination of whether a swimmer is of pusher or puller type follows from the sign of the scalar quantity

$$w(t) = \dot{\mathbf{q}}(t)^T \mathbf{S}(t) \dot{\mathbf{q}}(t), \tag{16}$$

in which $\dot{\mathbf{q}}(t)$ is the velocity of the swimmer at time t. More explicitly, a negative sign of w identifies a puller, whereas a positive sign of w corresponds to a pusher.

By applying the criterion above with reference to tractions and velocities computed with the BEM, we find that, on average, *E. gracilis* is a puller. Usually swimmers exploiting a single flagellum, such as *E. coli* or sperm cell, are pushers (see Refs. [16,19]), but the complex "spinning lasso" mechanism allows for a puller swimmer strategy. If we consider the actual behavior during the stroke we find that *E. gracilis* is a microswimmer of mixed type during a stroke, a fact in agreement with the observation of mixed pusher-puller behaviors in complex eukaryotic swimmers, as reported in Ref. [18].

The leading order approximation provides insights on the far field flow around a swimmer. However, the error introduced by this approximation becomes non-negligible in the near field, as shown in Ref. [57].

A more comprehensive approach to coarse-grain the flow field is to approximate the complex system of forces that

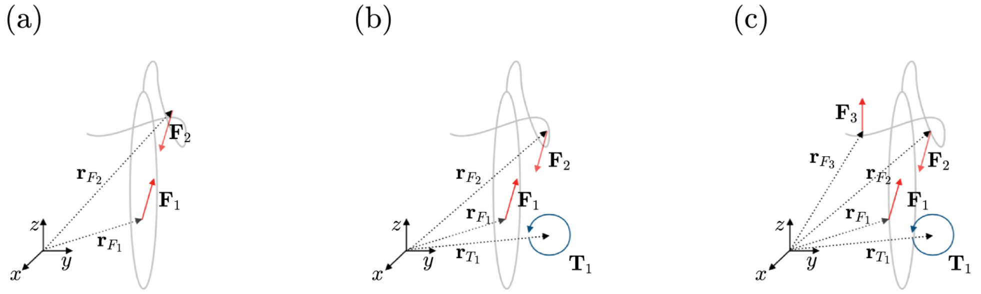

FIG. 6. Sketches of the three different singularity models we analyze for the reconstruction of the velocity field: (a) the Stokeslet doublet, (b) the two Stokeslets one Rotlet model (2S1R), and (c) the three Stokeslets one Rotlet model (3S1R).

the swimmer exerts on the surrounding fluid [19,57]. From a physical perspective, these are described by the traction $\mathbf{f}$ at the swimmer boundary—recall the balance equations (3)—and can be computed using the BEM mentioned in Sec. II. While this is the exact, infinite-dimensional parametrization of the forces exerted by a swimmer, it is often of interest to find a statically equivalent, finite-dimensional system of singularities (i.e., a system of finitely many concentrated forces and torques) capable of reproducing the main features of the surrounding fluid flow with sensible accuracy. In this way, one can arrive at a coarse-grained representation of the swimmer, and of the flow it induces, which is of great help in formulating a compact, conceptual picture of its interactions with the environment. This is the purpose of the present section, where we introduce and compare different singularity models for a swimming *E. gracilis*.

The flow field around microswimmers has often been approximated by a combination of fundamental solutions of Stokes flow. Applications of this approach range from swimming sperm cells, represented in Ref. [19] by means of force singularities (called Stokeslets), to swimming bacteria, whose flow field has been coarse grained through a combination of two Stokeslets (Stokeslet doublet) and two torque singularities (Rotlet doublet); see Refs. [16,58]. As an example of particular interest for the present study, the reconstruction of the fluid flow induced by *C. reinhardtii* has been successfully achieved in Ref. [37] by means of a system of three Stokeslets.

In view of the balance equations (3), we require the system of forces, $\mathbf{F}_i$, and of torques, $\mathbf{T}_i$, representing the actions of a swimmer on the surrounding fluid to satisfy

$$\sum_{i=1}^{N_F} \mathbf{F}_i = 0, \tag{17a}$$

$$\sum_{i=1}^{N_F} \mathbf{r}_{F_i} \times \mathbf{F}_i + \sum_{i=1}^{N_T} \mathbf{T}_i = \mathbf{0}, \tag{17b}$$

where the positions of each force $\mathbf{F}_i$ and torque $\mathbf{T}_j$ are identified using position vectors $\mathbf{r}_{F_i} = \mathbf{x}_i - \mathbf{O}$, $\mathbf{r}_{T_j} = \mathbf{x}_j - \mathbf{O}$.

The aforementioned forces and torques define the parameter set for each singularity approximation as

$$\boldsymbol{\theta}_{N_F,N_T} = \left(\mathbf{r}_{F_1}, \mathbf{F}_1, \dots, \mathbf{r}_{F_{N_F}}, \mathbf{F}_{N_F}, \mathbf{r}_{T_1}, \mathbf{T}_1, \dots, \mathbf{r}_{T_{N_T}}, \mathbf{T}_{N_T}\right), \tag{18}$$

and given a set of parameters, which represents N_F forces and N_T torques, the coarse-grained induced flow field is

$$\mathbf{v} = \mathbf{v}(\mathbf{x}|\boldsymbol{\theta}_{N_F,N_T}). \tag{19}$$

Given a set of positions in the space surrounding the swimmer we compute the optimal set of parameters through minimization of the error:

$$\bar{\boldsymbol{\theta}}^{t_i}_{N_F,N_T} = \underset{\boldsymbol{\theta}_{N_F,N_T}}{\arg\min}\, ||\mathbf{v}_{BEM}(\mathbf{x}, t_i) - \mathbf{v}(\mathbf{x}|\boldsymbol{\theta}_{N_F,N_T})||_{L_2}. \tag{20}$$

We consider three different, increasingly complex, approximations to coarse-grain the flow field: a Stokeslet doublet ($N_F = 2$, $N_T = 0$), two Stokeslets one Rotlet (2S1R, $N_F = 2$, $N_T = 1$) and three Stokeslets one Rotlet (3S1R, $N_F = 3$, $N_T = 1$). The sketches of these three models are shown in Fig. 6.

In order to find a reliable coarse-grained model for the flow field induced by *E. gracilis* in terms of a limited number of singularities, we consider the values of the fluid velocity as computed using the BEM on spherical shells surrounding the swimmer with internal and external radii $R_{\min}$ and $R_{\max}$, respectively. We use three different ranges to test the singularity approximations: nearby points between $R_{\min} = 1.5L_{\text{body}}$ and $R_{\max} = 5L_{\text{body}}$, intermediate points between $R_{\min} = 5L_{\text{body}}$ and $R_{\max} = 15L_{\text{body}}$, and faraway points between $R_{\min} = 15L_{\text{body}}$ and $R_{\max} = 25L_{\text{body}}$. We denote here by L_{body} the characteristic length of the swimmer ($\sim$50 μm), and consider a regular grid in spherical coordinates using 11 points along the radius, the polar and the azimuthal angle, for a total number of 1331 points for each spherical shell.

We use the Akaike Information Criterion [59] to assess the statistical quality of each model. The quantitative results relative to the mean velocity during the stroke for the three different models on the three different spherical shells are shown in Table I. We notice that, on far away points, the simple model of two Stokeslets provides the best approximation. We remark that this model is strictly related to the Stresslet introduced in (15). Hence, it is expected to provide a good approximation on distant points. On the contrary, the Stokeslet doublet is not sufficient to approximate the flow field on nearby and intermediate points. From the results of Table I, we conclude that the 2S1R model is the most suited on intermediate points while, on nearby points, it is statistically equivalent to the more complex 3S1R model. Thus, our analy-

TABLE I. Comparison in terms of the Akaike Information Criterion (AIC) between the three different approximations on nearby, intermediate, and far away points. We highlight in boldface the results corresponding to the best performing model. The labels (a), (b), and (c) refer to the three singularity models exploited for the reconstruction of the velocity field: the Stokeslet doublet, the two Stokeslets one Rotlet model (2S1R), and the three Stokeslets one Rotlet model (3S1R). The corresponding sketches are shown in Fig. 6.

Points	(a) Two Stokeslets	(b) 2S1R	(c) 3S1R
Nearby points	11714.9	**1892.9**	1922.3
Intermediate points	22.5	**13.2**	18.3
Far away point	**7.3**	12	39

sis suggests that approximations which are more complex than the 2S1R model are not needed for the representation of the flow field at distances larger than $1.5L_{\text{body}}$.

We now extend our analysis to the geometry of the flow field in close proximity to the cell body, in order to test whether the singularity models provide a realistic representation of the forces that *E. gracilis* exerts on the fluid. Of course, we only expect a qualitative agreement since, in the near field, the flow is strongly influenced by the presence of body and flagellum, with their actual shapes, which are not present in the flow field generated by the singularities. Furthermore, Stokes singularities lead to large velocity gradients that are not physical.

We optimize the corresponding velocity field $\mathbf{v}_{2S1R} = v_{2S1R}(\mathbf{x}|\boldsymbol{\theta}_{2,1})$ and $\mathbf{v}_{3S1R} = v_{3S1R}(\mathbf{x}|\boldsymbol{\theta}_{3,1})$ to match results from the BEM on points between $0.75L_{\text{body}}$ and $1.5L_{\text{body}}$, and we see that the 3S1R model reduces the error of more than 50% with respect to the 2S1R approximation. Results for the 3S1R model are shown at the center of Fig. 7 and highlight that two point forces are exploited by this approximation to model the action of the flagellum on the fluid.

For the sake of clarity, we report in Fig. 7 velocity fields in the xz-plane. Specifically, a comparison in terms of the mean velocity field between the 2S1R approximation (left column) and the BEM (right column) is shown in the first row of the figure. We notice a qualitative agreement in some features, such as the occurrence of significant velocities at the left hand side of the flagellum (where one Stokeslet is located). Also, the flow exhibits an off-axis puller signature (i.e., the axes of the flow are not aligned with the longitudinal axis of the body). Nevertheless, the two mean flows differ as a consequence of the coarse-graining due to the singularity approximation. In fact, the action of the flagellum is described by a single point force, with a significant loss of information in the mean velocity field. The 2S1R approximation also introduces a visible peak in the velocity field at the center of the cell body. The rationale behind it is twofold: (1) the torque resulting from the tangential forces induced by the rotations of the body is approximated by a concentrated Rotlet and (2) the forces exerted by the flagellum are more complex than what can be captured by a single Stokeslet, with part of them contributing to the Stokeslet near the body center. The resulting effect is a

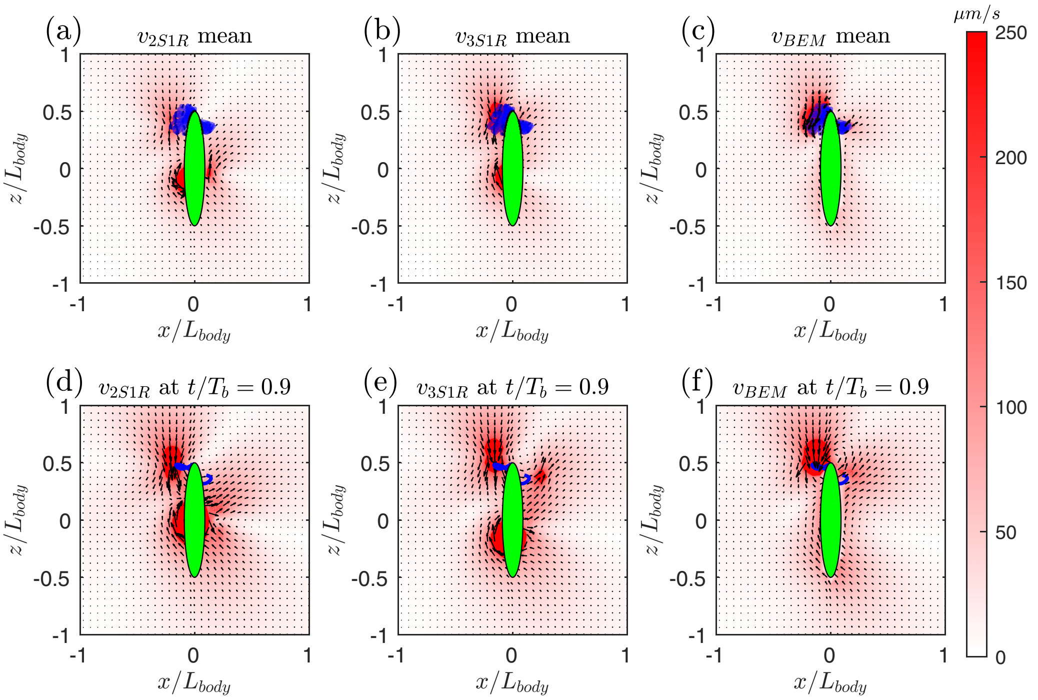

FIG. 7. Qualitative flow field comparison in the xz-plane between the BEM (third column) and two singularity approximations: 2S1R used to approximate the far field (left column) and 3S1R (middle column). The first row represents the mean velocity, while the second reports the velocity computed for $t/T_b = 0.9$. The colormap represents the magnitude of the velocity field as projected on the xz-plane, while the quivers show the velocity projected on the plane. In all the figures, we superimpose in green the cell body and in blue the flagellar shapes. In particular, all the 10 flagellar shapes are shown in (a), (b), and (c), while only the flagellar shape relative to $t/T_b = 0.9$ is reported in (d), (e), and (f).

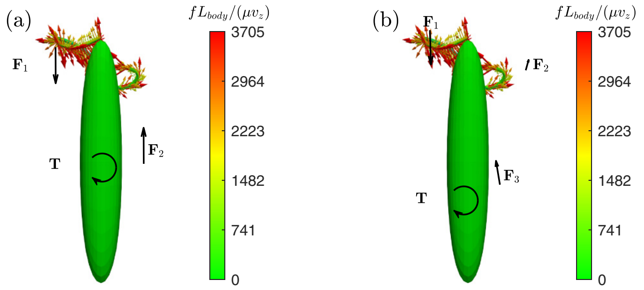

FIG. 8. Qualitative comparison in the xz-plane between the BEM tractions and the singularity systems 2S1R (a) and 3S1R (b). The torques represented in black are projections along the y axis. Black arrows on the xz-plane complement the representation of the singularity systems. The colormap is for the magnitude $f = |\mathbf{f}|$ of the BEM tractions $\mathbf{f}$ on the xz-plane.

strong singularity in the velocity field near the body center, with velocities having much higher magnitudes than those from the BEM.

This fact is further emphasized by Fig. 8, where the 2S1R (left) and the 3S1R (right) models are compared. In particular, the figure shows the respective systems of forces as superimposed to the traction field **f** from the BEM. Interestingly, we notice that an increase in the complexity of the model in terms of number of singularities leads to a more accurate representation of the continuous traction field. In passing, we notice that a better approximation in the near field could be achieved by further increasing the number of singularities, although at the expense of increasing the number of parameters to account for in modeling the system.

To prove the effectiveness of the qualitative reconstruction in the near field, we analyze in the second row of Fig. 7 the flow field at time $t/T_b = 0.9$. This exhibits a clear puller signature with, in addition, rotational flows induced by the eccentricity of the flagellum. Both these facts are recovered by the two singularity approximations. Only the 3S1R model, however, is able to capture a feature revealed by the BEM analysis, namely, that the forces exerted by the flagellum are large and propulsive (directed downwards) near the proximal end, while they are smaller but resistive (directed upwards) at the distal end. This is clearly visible in Fig. 8, where we recall that the tractions exerted by the flagellum on the fluid, as computed using the BEM, are compared with the two systems of singularities described above. Returning to Fig. 7, we still recognize a significant peak in the velocity magnitude at the center of the body. As discussed earlier, this is induced by having concentrated at a singular point all the distributed forces exerted by the cell body.

From our analysis, we conclude that the 2S1R approximation provides a satisfactory way to rationalize the flow field induced by a sample of swimming *E. gracilis* at distances between $1.5L_{\text{body}}$ and $15L_{\text{body}}$. To arrive at a better approximation in the immediate proximity of the cell body we had to account for more singularities to capture the complexity of the action of the flagellum on the surrounding fluid, as demonstrated by the 3S1R approximation.

V. CONCLUSIONS

The analysis of the flow fields induced in the surrounding fluid offers insight on the swimming behavior of microorganisms. In this work we have presented a numerical reconstruction of the three-dimensional flow field generated by a specimen of *E. gracilis* swimming using the "spinning lasso" flagellar mechanism, a nonplanar waveform. We have accomplished this by reconstructing the history of flagellar shapes and shape velocities, and then computing the resulting flows by solving numerically the Stokes equations with a boundary element method. The experimentally measured translational and angular velocities of the swimmer, and its observed trajectories are reproduced very accurately by our procedure. This fact provides a strong argument supporting our reconstruction of the swimming stroke.

Furthermore, we have validated our numerical reconstruction of the flow field against experimental measurements obtained with the general defocusing particle tracking method. This technique allows to track the three-dimensional position of passive tracer particles dispersed in the fluid, and hence to reconstruct the complete flow field. This is needed here since *E. gracilis* uses a nonplanar flagellar beat. Looking at the time- and azimuthally averaged velocity fields, we could identify three characteristic flow structures for all the three velocity components, both in the numerical and in the experimental data. The good agreement between experimental data and numerical results justifies the use of the numerical model (our synthetic stroke) to analyze in more detail the swimmer mechanism of real *Euglena* cells.

We have then analyzed the flow fields, computed by solving numerically the Stokes equations via BEM and using as input the synthetic stroke. We have considered the leading order term of the multipole expansion and we have found that *E. gracilis* can be idealized as an off-axis puller. Its instantaneous character during the stroke oscillates between a puller and a pusher behavior, similarly to what has been observed for other micro-organisms such as sperm cells and *C. reinhardtii*. We have deepened our analysis by coarse-graining the flow fields in terms of a few dominant Stokes flow singularities. We find that a system of two eccentric Stokeslets and one Rotlet is able to approximate well the velocity field away from the body, and captures some of the main features of the swimming mechanism of the organism. Moreover, the BEM analysis shows that the flagellum may exert forces that change orientation along its length (e.g., propulsive forces near the proximal end and resistive ones at the distal end). To capture this effect and, more generally, to represent adequately the signature on the generated flow left by flagella and cilia that do not beat in a single plane, more complex systems of singularities would be needed. We hope that our study may motivate also others to investigate the question of which systems of singularities may be effective in coarse-graining the flows associated with the three-dimensional trajectories that have attracted interest in the recent bio-physical literature on microswimmers [3,8,13,24–28].

We notice that results of the present study may open the way to future studies on the internal dynamics of the flagellum resolving the interactions between axoneme and molecular motors and their regulation as in Ref. [60].

ACKNOWLEDGMENTS

This work has been supported by the ERC Advanced Grant No. 340685 MicroMotility. M.R. acknowledges funding from the European Union's Horizon 2020 research and innovation program under the Marie Sklodowska-Curie Grant Agreement No. 713683 (COFUNDfellowsDTU).

---

[1] B. S. Leander, G. Lax, A. Karnkowska, and A. G. B. Simpson, *Euglenida*, in *Handbook of the Protists*, edited by J. Archibald *et al.* (Springer, Cham, 2017), pp. 1–42.

[2] G. Noselli, A. Beran, M. Arroyo, and A. DeSimone, Swimming *Euglena* respond to confinement with a behavioural change enabling effective crawling, Nat. Phys. **15**, 496 (2019).

[3] A. C. H. Tsang, A. T. Lam, and I. H. Riedel-Kruse, Polygonal motion and adaptable phototaxis via flagellar beat switching in the microswimmer *Euglena gracilis*, Nat. Phys. **14**, 1216 (2018).

[4] M. Arroyo and A. DeSimone, Shape control of active surfaces inspired by the movement of euglenids, J. Mech. Phys. Solids **62**, 99 (2014).

[5] M. Arroyo, L. Heltai, D. Millan, and A. DeSimone, Reverse engineering the euglenoid movement, Proc. Natl. Acad. Sci. USA **109**, 17874 (2012).

[6] Y. Chen, Flagellum malfunctions trigger metaboly as an escape strategy in *Euglena gracilis*, bioRxiv 863282 (2019).

[7] K. M. Digumarti, A. T. Conn, and J. Rossiter, EuMoBot: Replicating euglenoid movement in a soft robot, J. R. Soc. Interface **15**, 20180301 (2018).

[8] M. Rossi, G. Cicconofri, A. Beran, G. Noselli, and A. DeSimone, Kinematics of flagellar swimming in *Euglena gracilis*: Helical trajectories and flagellar shapes, Proc. Natl. Acad. Sci. USA **114**, 13085 (2017).

[9] E. A. Gaffney, H. Gadelha, D. J. Smith, J. R. Blake, and J. C. Kirkman-Brown, Mammalian sperm motility: Observation and theory, Annu. Rev. Fluid Mech. **43**, 501 (2011).

[10] J. S. Guasto, R. Rusconi, and R. Stoker, Fluid mechanics of planktonic microorganisms, Annu. Rev. Fluid Mech. **44**, 373 (2012).

[11] R. E. Goldstein, Green algae as model organisms for biological fluid dynamics, Annu. Rev. Fluid Mech. **47**, 343 (2015).

[12] K. Y. Wan, Ciliate biology: The graceful hunt of a shape-shifting predator, Curr. Biol. **29**, R1174 (2019).

[13] J. F. Jikeli, L. Alvarez, B. M. Friedrich, L. G. Wilson, R. Pascal, R. Colin, M. Pichlo, A. Rennhack, C. Brenker, and U. B. Kaupp, Sperm navigation along helical paths in 3D chemoattractant landscapes, Nat. Commun. **6**, 7985 (2015).

[14] T. Kiørboe, H. Jiang, R. J. Gonçalves, L. T. Nielsen, and N. Wadhwa, Flow disturbances generated by feeding and swimming zooplankton, Proc. Natl. Acad. Sci. USA **111**, 11738 (2014).

[15] G. Gompper, R. G. Winkler, T. Speck, A. Solon, C. Nardini, F. Peruani, H. Löwen, R. Golestanian, U. B. Kaupp, L. Alvarez *et al.*, The 2020 motile active matter roadmap, J. Phys.: Condens. Matter **32**, 193001 (2020).

[16] E. Lauga, Bacterial hydrodynamics, Annu. Rev. Fluid Mech. **48**, 105 (2016).

[17] K. Drescher, K. C. Leptos, and R. E. Goldstein, How to track protists in three dimensions, Rev. Sci. Instrum. **80**, 014301 (2009).

[18] G. S. Klindt and B. M. Friedrich, Flagellar swimmers oscillate between pusher- and puller-type swimming, Phys. Rev. E **92**, 063019 (2015).

[19] K. Ishimoto, H. Gadêlha, E. A. Gaffney, D. J. Smith, and J. Kirkman-Brown, Coarse-Graining the Fluid Flow Around a Human Sperm, Phys. Rev. Lett. **118**, 124501 (2017).

[20] T. Ishikawa, G. Sekiya, Y. Imai, and T. Yamaguchi, Hydrodynamic interactions between two swimming bacteria, Biophys. J. **93**, 2217 (2007).

[21] H. Shum, E. A. Gaffney, and D. J. Smith, Modelling bacterial behavior close to a no-slip plane boundary: The influence of bacterial geometry, Proc. R. Soc. London, Ser. A **466**, 1725 (2010).

[22] H. Shum and E. A. Gaffney, Hydrodynamic analysis of flagellated bacteria swimming near one and between two no-slip plane boundaries, Phys. Rev. E **91**, 033012 (2015).

[23] D. Pimponi, M. Chinappi, P. Gualtieri, and C. M. Casciola, Hydrodynamics of flagellated microswimmers near free-slip interfaces, J. Fluid Mech. **789**, 514 (2016).

[24] T. J. Carroll, 3D reconstruction of human sperm kinematics, Senior thesis, Tufts University, Medford, MA (2015).

[25] P. Sartori, V. F. Geyer, J. Howard, and F. Jülicher, Curvature regulation of the ciliary beat through axonemal twist, Phys. Rev. E **94**, 042426 (2016).

[26] D. Helene *et al.*, Motility and phototaxis of *Gonium*, the simplest differentiated colonial alga, Phys. Rev. E **101**, 022416 (2020).

[27] H. Gadêlha, P. Hernández-Herrera, F. Montoya, A. Darszon, and G. Corkidi, Human sperm uses asymmetric and anisotropic flagellar controls to regulate swimming symmetry and cell steering, Sci. Adv. **6**, eaba5168 (2020).

[28] D. Cortese and K. Y. Wan, Control of helical navigation by three-dimensional flagellar beating, bioRxiv 315606 (2020).

[29] J. Gray and G. J. Hancock, The propulsion of sea-urchin spermatozoa, J. Exp. Biol. **32**, 802 (1955).

[30] J. Lighthill, Flagellar hydrodynamics, SIAM Rev. **18**, 161 (1976).

[31] B. Rodenborn, C. H. Chen, H. L. Swinney, B. Liu, and H. P. Zhang, Propulsion of microorganisms by a helical flagellum, Proc. Natl. Acad. Sci. USA **110**, E338 (2013).

[32] N. Giuliani, L. Heltai, and A. DeSimone, Predicting and optimizing microswimmer performance from the hydrodynamics of its components: The relevance of interactions, Soft Robot. **5**, 410 (2018).

[33] N. Giuliani, L. Heltai, and A. DeSimone, BEMStokes: A Boundary Element Method solver for micro-swimmers, https://github.com/mathLab/BEMStokes (2021).

[34] N. Giuliani, L. Heltai, and A. DeSimone, PostProcess-BEMStokes: A Boundary Element Method post processor for micro-swimmers, https://github.com/mathLab/PostProcessBEMStokes (2021).

[35] R. Barnkob, C. J. Kähler, and M. Rossi, General defocusing particle tracking, Lab Chip **15**, 3556 (2015).

[36] M. Rossi and C. J. Kähler, Optimization of astigmatic particle tracking velocimeters, Exp. Fluids **55**, 1 (2014).

[37] K. Drescher, R. E. Goldstein, N. Michel, M. Polin, and I. Tuval, Direct Measurement of The Flow Field Around Swimming Microorganisms, Phys. Rev. Lett. **105**, 168101 (2010).

[38] V. F. Geyer, F. Jülicher, J. Howard, and B. M. Friedrich, Cell-body rocking is a dominant mechanism for flagellar synchronization in a swimming alga, Proc. Natl. Acad. Sci. USA **110**, 18058 (2013).

[39] B. M. Friedrich, I. H. Riedel-Kruse, J. Howard, and F. Jülicher, High-precision tracking of sperm swimming fine structure provides strong test of resistive force theory, J. Exp. Biol. **213**, 1226 (2010).

[40] K. T. Wu, Y. T. Hsiao, and W. Y. Woon, Entrapment of pusher and puller bacteria near a solid surface, Phys. Rev. E **98**, 052407 (2018).

[41] S. Kim and S. J. Karilla, *Microhydrodynamics: Principles and Selected Applications* (Dover Publications, New York, 1991).

[42] G. Dal Maso, A. DeSimone, and M. Morandotti, One-dimensional swimmers in viscous fluids: Dynamics, controllability, and existence of optimal controls, ESAIM: COCV **21**, 190 (2015).

[43] G. Dal Maso, A. DeSimone, and M. Morandotti, An existence and uniqueness result for the motion of self-propelled microswimmers, SIAM J. Math. Anal. **43**, 1345 (2011).

[44] M. Gurtin, *An Introduction to Continuum Mechanics*, Mathematics in Science and Engineering (Academic Press, New York, 1982).

[45] E. M. Purcell, Life at low Reynolds number, Am. J. Phys. **45**, 3 (1977).

[46] N. Giuliani, Modelling fluid structure interaction problems using boundary element method, Ph.D. thesis, SISSA, Scuola Internazionale Superiore di Studi Avanzati (2017).

[47] See Supplemental Material at http://link.aps.org/supplemental/10.1103/PhysRevE.103.023102 for a detailed description of the numerical method and the experimental setup.

[48] A. Quarteroni, *Numerical Mathematics* (Springer, Berlin, 2007).

[49] M. A. Branch, T. F. Coleman, and Y. Li, A subspace, interior, and conjugate gradient method for large-scale bound-constrained minimization problems, SIAM J. Sci. Comput. **21**, 1 (1999).

[50] J. S. Guasto, K. A. Johnson, and J. P. Gollub, Oscillatory Flows Induced by Microorganisms Swimming in Two Dimensions, Phys. Rev. Lett. **105**, 168102 (2010).

[51] T. Ogawa, S. Izumi, and M. Iima, Statistics and stochastic models of an individual motion of photosensitive alga *Euglena gracilis*, J. Phys. Soc. Jpn. **86**, 074401 (2017).

[52] R. Barnkob and M. Rossi, General defocusing particle tracking: Fundamentals and uncertainty assessment, Exp. Fluids **61**, 110 (2020).

[53] C. Cierpka, M. Rossi, R. Segura, and C. Kähler, On the calibration of astigmatism particle tracking velocimetry for microflows, Meas. Sci. Technol. **22**, 015401 (2010).

[54] M. Rossi and R. Barnkob, A fast and robust algorithm for general defocusing particle tracking, Measurement Science and Technology, Meas. Sci. Technol. **32**, 014001 (2020).

[55] R. Di Leonardo, J. Leach, H. Mushfique, J. Cooper, G. Ruocco, and M. Padgett, Multipoint Holographic Optical Velocimetry in Microfluidic Systems, Phys. Rev. Lett. **96**, 134502 (2006).

[56] P. G. Dehnavi, D. Wei, M. E. Aubin-Tam, and D. S. W. Tam, Optical tweezers-based velocimetry: A method to measure microscale unsteady flows, Exp. Fluids **61**, 202 (2020).

[57] K. Ishimoto, E. A. Gaffney, and B. J. Walker, Regularized representation of bacterial hydrodynamics, Phys. Rev. Fluids **5**, 093101 (2020).

[58] J. Hu, M. Yang, G. Gompper, and R. G. Winkler, Modelling the mechanics and hydrodynamics of swimming *E. coli*, Soft Matter **11**, 7867 (2015).

[59] H. Akaike, A new look at the statistical model identification, IEEE Trans. Autom. Control **19**, 716 (1974).

[60] I. H. Riedel-Kruse, A. Hilfinger, J. Howard, and F. Jülicher, How molecular motors shape the flagellar beat, HFSP J. **1**, 192 (2007).